POLITECNICO DI TORINO
Repository ISTITUZIONALE

CFD analysis of internal ventilation in high-speed Human Powered Vehicles

(Article begins on next page)

19 April 2024

CFD analysis of internal ventilation in high-speed Human Powered Vehicles.

Abstract When dealing with fully faired Human Powered Vehicles (HPVs) for speed or endurance record attempts, the need for internal ventilation of the rider arises. Different solutions have been proposed in the literature and in practice by designers and builders of these bicycles. The present paper proposes an analytical approach to design the frontal air inlet according to the VO_2max of the rider in speed competitions. A 3D computational fluid dynamics (CFD) model is presented to analyze the external and internal flow interaction with respect to three design parameters: the presence of wheel-covers, the location of the rear vent and its geometry. The CFD results predict the wheel-covers save 23 W of aerodynamic power at 125 km/h. A secondary but significant design parameter is the rear vent position, that can provide a further reduction of 11 W at 125 km/h if properly located. Finally, the effect of the rear vent geometry was below the model confidence level, resulting in a likely negligible design parameter.

1 Introduction

Computational fluid dynamics (CFD) is becoming a popular analysis method in many sport disciplines. This numerical technique for solving an approximate form of the Navier-Stokes equations has been initially developed in the Aerospace and Automotive industrial fields [1–4]. Thanks to the current accessibility of high computational resources at affordable prices, CFD is applied to a wide range of sport related problems in nautical disciplines, from America's Cup [5] to kayak [6] and rowing boats [7–9], in swimming [10–12] and as a well-established method in cycling [13–20].

A specific and particular context where CFD is becoming a helpful tool is the design of Human Powered Vehicles (HPVs). Even if not classified among classical sport disciplines and banned from traditional cycling, HPVs offer an interesting range of competitions all over the world from local races organized by national associations to the world championships and challenges sanctioned by the international organizations IHPVA (International Human Powered Vehicle Association, US based) [21] and WHPVA (World Human Powered Vehicle Association, EU based) [22]. While the acronym HPV indicates a wide category of vehicles, it mainly refers to recumbent bicycles and tricycles, that are showing a slow but constant growth in popularity [23–25] since the end of the last century. The recumbent cycling position is mainly appreciated for the lower aerodynamic drag, for the reduced load on the vertebral column and the comfortably distributed pressure on the large seat area. The sum of these advantages allows further and faster travel for the same level of effort. The high-speed class to which this article refers is represented by the vehicles competing in the World Human Powered Speed Championship (WHPSC) [26] yearly held in Battle Mountain (Nevada, US). Here, the high-speed is calculated by timing a segment of 200 m at the end of a 8 km run-up (average slope −0.6%), resulting in a so called "flying start" race.

HPV internal ventilation has been often discussed in literature. Nobile provided a general calculation for the air intake and outlet area, together with a practical guide to design the diffuser cone which is needed to recover the pressure at the front nose inlet [27]. Here, the required inlet area is calculated by dividing the volume flow rate through the inlet by the vehicle velocity. However, no details are provided on how the air requirement for the rider is

calculated and the velocity is arbitrarily fixed at a minimum value of 1.5 m/s. Drela provided an analytical equation to calculate the additional drag given by a front nose air inlet [28]. In this case, no numerical values were given and the formula suggests that the minimum impact on drag is obtained by maximizing the air inlet area and minimizing the outlet one. However, this approach does not provide a specific reference on how to size the ventilation system for a desired air flow at a given speed, and could mislead the designer to oversize the inlet hole. A more detailed approach was given by Schreur, but with a specific focus on endurance races where heat removal and cockpit temperature control play a dominant role over breathing requirements [29].

This paper proposes a design method for the frontal air inlet in high-speed HPVs, considering the oxygen needs of the rider in maximal effort conditions. Then, the CFD analysis is applied to investigate the effects of wheel covers, rear vent location and geometry on the overall drag of a high-speed HPV case study.

2 Internal ventilation requirements

Enclosing the rider inside an aerodynamic shell creates the need for a ventilation system having the following requirements:

- to provide the required amount of oxygen for the planned effort and external conditions;
- to cool down the inner temperature;
- to cool the braking system (usually discs);
- to remove the water vapour generated by the rider and to prevent condensation on windows (if any);
- to minimize aerodynamic drag.

An additional requirement is provided by the IHPVA competition rules excluding the use of any additional source of energy for propulsion and cooling. Active fan ventilation is allowed only if the required energy is drained from muscular power, which means it is subtracted from the amount available for the vehicle propulsion. These conditions drive the design to the most natural solution of one or more air intakes and outlets working with the vehicle speed.

In order to satisfy the oxygen requirement, the overall need in terms of air flow rate has to be estimated. This parameter depends on the purpose of the vehicle and on the kind of effort required by the rider. As mentioned before, the case of endurance disciplines (such as the one hour record) requires large ventilation for cooling and drying the rider. In the present work, the acceleration and sprint effort of the WHPSC 200 m flying start is considered which is different from the 200 m flying start in track or standard road cycling. In standard cycling, a relatively short distance of less than 1 km is sufficient to accelerate the rider up to a high-speed of 77.03 km/h (UCI World Record by François Pervis, 2013) with an overall effort duration of less than 1 minute. In HPV high-speed competitions, the rider needs a longer run-up for a duration of 5-6 minutes to reach a top speed of 144.17 km/h (IHPVA World Record by Todd Reichert, 2016). In Fig. 1, the power and speed of a WHPSC high-speed attempt [30] are plotted with respect to the run-up time.
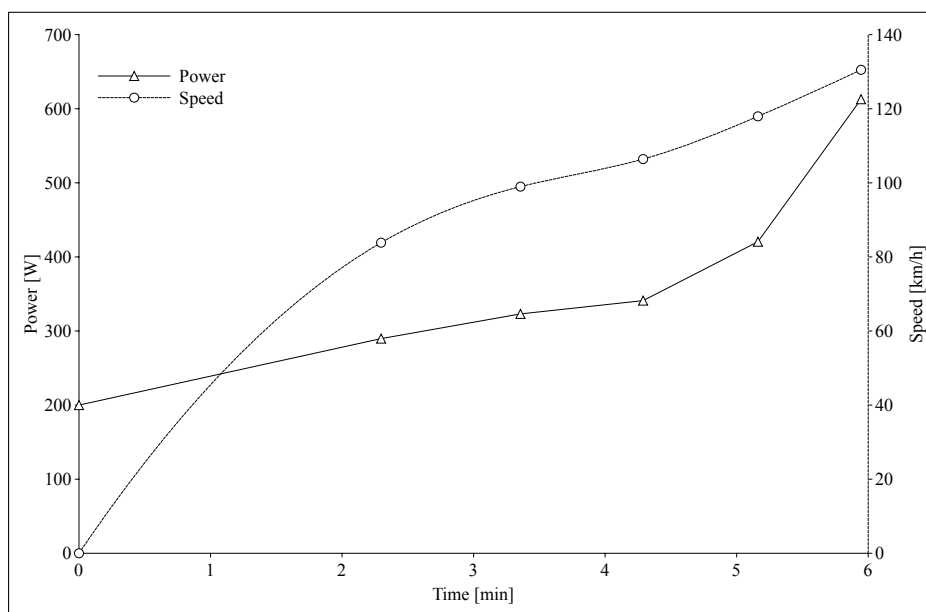

Fig. 1 Power and speed during a WHPSC run-up, extrapolated from [30] assuming 200 W as initial power.

For a high-speed vehicle and maximal effort conditions a first estimation of the needed flow can be obtained from

$$\varphi = f \cdot \frac{m \cdot \text{VO}_2\text{max}}{\%O_{2,IN} - \%O_{2,OUT}} \tag{1}$$

where φ is the needed internal air turnover (flow rate), VO_2max is the maximum oxygen consumption rate of the rider normalized by his/her mass m, $\%O_{2,IN}$ and $\%O_{2,OUT}$ are the oxygen fractions in inhaled and exhaled air, respectively. A factor f has been introduced to account for the portion of air passing through the cockpit that is used effectively for breathing.

As an example, considering a first class athlete of 70 kg with a VO_2max of 80 ml/(kg·min) gives up to 5.6 l/min of O_2. Considering typical fractions of 21% for $O_{2,IN}$ and 16% for $O_{2,OUT}$, an overall flow rate of 112 l/min is obtained, which is slightly more than the 100 l/min reported by Kyle et al. [30] and less than the 150 l/min given by Gong et al. [31]. However, considering flow dispersion, $f = 1.2$ is used, leading to $\varphi = 134.4$ l/min. This represents the air need estimate during a maximal sprint, that, for high-speed vehicles, is usually starting above 90 km/h.

Air flow entering through the inlet at a given speed can be represented, in its upstream configuration, as an ideal cylinder (Fig. 2). The length L of the cylinder is directly proportional to the vehicle speed v, while its diameter D is less obvious. Compression and acceleration effects result in $D \geq d$.
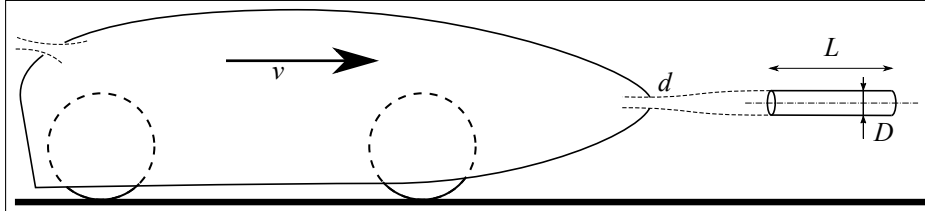

Fig. 2 Schematic representation of the virtual cylinder of air entering the vehicle.

From geometrical considerations, the required inlet diameter can be calculated as

$$d = \eta \cdot D = \eta \cdot \sqrt{\frac{4 \cdot \varphi}{\pi \cdot v}} \tag{2}$$

where v is the vehicle reference speed and η is the air compression ratio ($0 \leq \eta \leq 1$) relating d and D. The value of η is expected to depend on the speed, since the pressure boundary conditions at the nose of the vehicle are varying with it. However, given the typical range of speed for HPVs, a relatively small compression is expected, with $\eta \sim 0.9$. In the following, a reference value for η will be calculated for a specific case study through CFD analysis. With $\varphi = 134.4$ l/min, $v = 90$ km/h and $\eta = 0.9$, the resulting inlet hole diameter becomes $d = 9.6$ mm.

3 Models and methods

A CFD model of a high-speed HPV was developed by using StarCCM+$^{\circledR}$ [32]. As shown in Fig. 3(a), the geometry was imported from the CAD and meshed, including external fairing, rotating wheels and tires, internal structure, diffuser and collector tube for the air intake, and a stationary rider mannequin.

The selected HPV model was originally designed with $f = 3$ to be suitable for endurance training sessions at lower average speed. As a consequence it had an air inlet cross section diameter of 18 mm, that can provide 336 l/min of air at 65 km/h.

3.1 CFD model implementation and validation

3.1.1 Assumptions and boundary conditions

The study was performed considering a speed of 125 km/h in open-road conditions. A simulation domain of $25 \times 6 \times 5$ m as in Fig. 3(b) was used for a vehicle of $2.8 \times 0.5 \times 0.8$ m referring to length, width and height, respectively. Moving ground and wheel rotation were imposed as boundary conditions for the flow to reproduce a realistic road context.

To simplify the numerical model all the transmission components were not included. Moreover, rider's feet and legs inside the fairing were considered static, while surface roughness and imperfect junctions were neglected.

The meshing procedure was tuned in order to find a compromise between the result reliability and the calculation time with the available computational resources. Since the
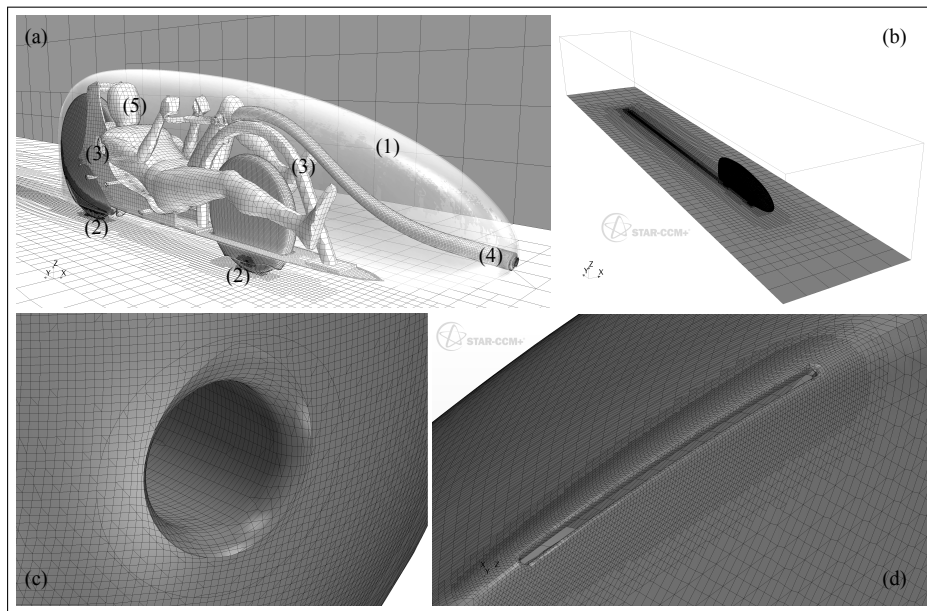
Fig. 3 Model volumetric mesh: vehicle overview (a) including fairing (1), wheels (2), internal structures (3), air inlet collector tube (4) and rider (5), overall CFD domain (b), round fillet mesh detail for the air inlet (c) and outlet (d).

flow inside the fairing is not expected to show strong boundary effects, the rider and the internal structures were assigned to a target cell size of 10 mm and without a prism layer. A finer mesh, including a 5 mm boundary layer with three prismatic cells, was applied to the external fairing, wheels and air inlet tube, to calculate the near-wall flow in these higher velocity gradient regions. As shown in Fig. 3(c) and Fig. 3(d), two mesh refinement areas with a target size of 1.5 mm were needed at the air inlet hole and at the outlet cut to improve the model geometrical accuracy. Finally, to obtain a detailed evaluation of the wake flow, a 6 m trimmer refinement mesh was imposed behind the vehicle, as shown in Fig. 3(b). A summary of the model general data is shown in Table 1.

Table 1 CFD model data summary.

Number of cells	6×10^6	
Reference air density	1.18	kg/m^3
Reference pressure	101325	Pa
Simulation domain inlet and ground speed	125	km/h
Flow model	Segregated	
Wall treatment	All y^+	

3.1.2 Turbulence model selection

In CFD analysis a turbulence model which is representative of the real flow conditions is needed. While high-speed HPVs are often designed aiming at extended laminarity, some shapes and manufacturing inaccuracy can produce a predominant turbulent boundary layer.

To verify and select the proper turbulence model, two boundary layer formulations were applied and simulated on the original geometry. The A_{lam} model considered k-ω turbulence with γ-Re_θ laminar/turbulent transition for the external flow [33]. The A_{turb} model used the Spalart-Allmaras fully turbulent formulation [34]. For validation purposes, the results were compared to the drag obtained with a coast-down experiment on a real HPV with no wheel-covers [35–38].

As shown in Table 2, model A_{lam} strongly underestimated the drag (–214 W), while model A_{turb} fell within the confidence interval of the experiment with a relatively small gap from the central value (–7 W). As a consequence, a confidence interval of $\pm 1.3\%$ (± 7 W over 531 W) was assumed in the following for simulations with a turbulent boundary layer.

Table 2 Measured and calculated drag force, coefficient and power at 125 km/h.

Model	F_d [N]	C_d	P_d [W]
Testing [35]	15.49±0.37	0.0834±0.010	538±13
CFD A_{lam}	9.34	0.0505	324
CFD A_{turb}	15.30	0.0826	531

The result of the fully turbulent model indicated that the rough finishing of the HPV makes an extended laminar boundary layer on its surface unlikely. As a consequence, in the following analyses the Spalart-Allmaras formulation was adopted as the turbulence model. The A_{turb} model was used as starting point for the subsequent optimization and is referred to as model A.

3.1.3 Mesh sensitivity analysis and wall treatment

A sensitivity analysis was conducted to assess the model reliability with respect to changes in the base size of the mesh. For each local refinement region, the mesh size in StarCCM+$^{®}$

is expressed as a percentage of the so called "base size", that allows for overall scaling of the cell density. Starting from an initial base size of 100 mm, the cell size ranged from 80 to 120 mm ($\pm 20\%$). The drag was independent of the mesh size, with variations of ± 0.024 N, corresponding to $\pm 0.16\%$ of the 100 mm base cell size model (15.30 N).

A requirement of the Spalart-Allmaras turbulence model for the simulation accuracy is to have

$$y^+ \leq 1$$
$$\text{or}$$
$$30 \leq y^+ \leq 200$$

(3)

where y^+ is the non-dimensional wall distance [39] defined as

$$y^+ = \frac{y}{\nu} \cdot \sqrt{\frac{\tau_w}{\rho}}$$

(4)

where y is the distance of a point from the nearest wall, ν the kinematic viscosity, τ_w the wall shear stress, and ρ the fluid density at the wall.

To provide an accurate solution of the boundary layer flow, the solver requires $y^+ \leq 1$ or $30 \leq y^+ \leq 200$. By respecting these constraints, full integration or analytical wall function are automatically applied within their maximum reliability domains [32].

For the simulated models 97% of the cells around the fairing boundary shows $y^+ \leq 1$ and 3% has $1 < y^+ \leq 1.4$. The internal part boundaries show 95% of the cells at $30 \leq y^+ \leq 200$ and 5% at $22 \leq y^+ < 30$.

Although further refinements could be achieved by improving the mesh quality, the values were considered robust enough for the purpose of this comparative study.

3.2 Subcases and configurations

An objective of the study was to quantify the impact of wheel-covers on the overall air drag. As a consequence, a subcase B was derived from the same geometry of model A by adding the cover surfaces with an offset of 8 mm from both front and rear wheels. The second part

of the study was focused on location and geometry of the rear air outlet. Subcase model C considered a different position of the air outlet to estimate its influence. The height from ground (H), both longitudinal placement and orientation (α) of the air outlet were determined by the fairing lateral profile. Models D, E, F and G were implemented by introducing variations of the air outlet geometry.

The study was limited to a rectangular air outlet cut as represented in Fig. 4. The area (A_o) and aspect ratio ($R = L/W$) of the rear vent were selected as design variables. The geometrical values implemented in each model are summarized in Table 3.
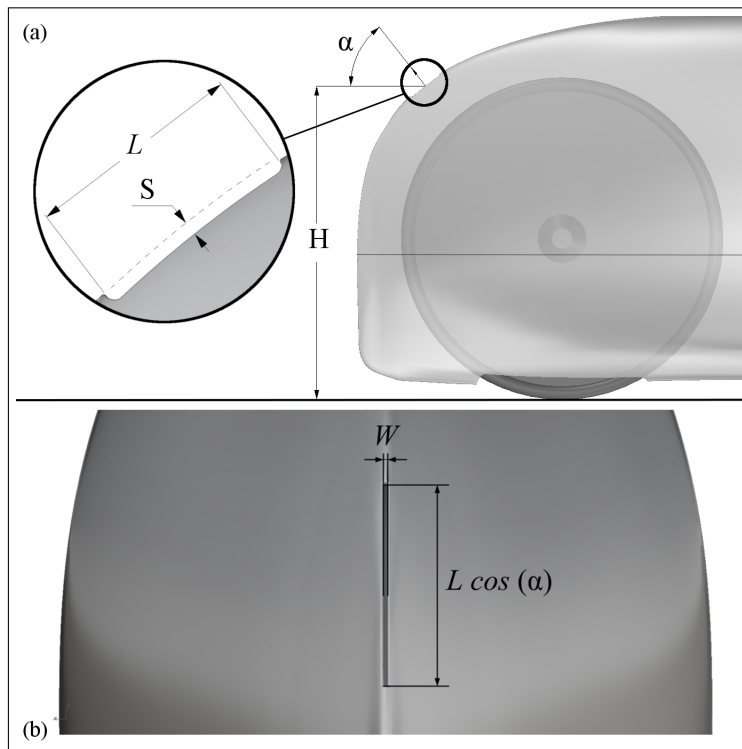

Fig. 4 Air outlet cut reference measures: side view (a) and detail of back view (b).

Table 3 Air outlet cut geometry and position for each model.

Model	A_o [mm^2]	R	L [mm]	W [mm]	H [mm]
A, B	450	50	150	3	660
C	450	50	150	3	420
D	450	10	67	7	420
E	200	30	116	3	420
F	700	30	145	5	420
G	450	30	116	4	420

4 Results and discussion

The mesh sensitivity analysis converged after about 1600 iterations (CPU time 59 hours, user time 7.6 hours) on a Dell Precision T7400 workstation with $2\times$ Intel$^®$ Xeon$^®$ quad-core and 16 GB RAM. All subsequent simulations were run on 64 cores (AMD Opteron 2.3 GHz) through a high performance computing cluster. Here, each simulation required around 54 minutes to converge with an overall CPU time of 56 hours.

The drag force and coefficient for each model configuration are summarized in Table 4. By multiplication of the drag force by the simulated speed, the power dissipated by aerodynamic resistance can be obtained and compared as in Fig. 5.

Table 4 Calculated drag force, coefficient and power at 125 km/h for each model configuration.

Model	F_d [N]	C_d
A	15.30	0.0826
B	14.62	0.0789
C	14.30	0.0772
D	14.23	0.0768
E	14.19	0.0766
F	14.34	0.0774
G	14.18	0.0765

4.1 The role of static wheel-covers

The results reported in Fig. 5 indicate that wheel-covers play an important role and their addition can save up to 23 W of power at 125 km/h. As shown in Fig. 6(a) and Fig. 7, the rotation of the uncovered rear wheel creates a depression near the air outlet and makes it to
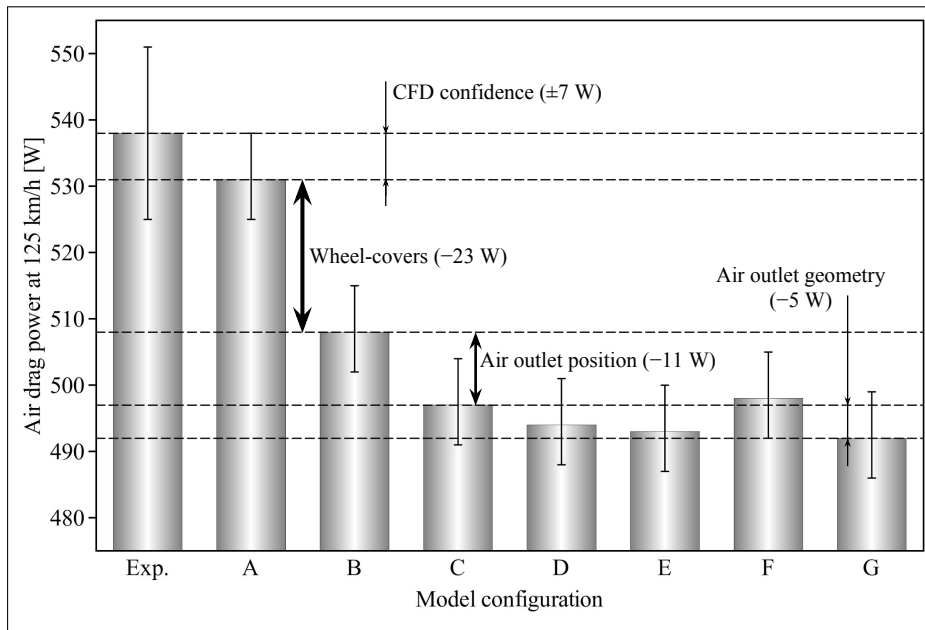
Fig. 5 Summary of the calculated air drag power for each model configuration and contribution of each investigated aspect.

work effectively as an inlet. The air flowing on the external surface is sucked in and the role of outlet is delegated to the wheel openings. The CFD simulation of model B confirms that wheel-covers allow the air to exit the outlet, as shown in Fig. 6(b).

According to the simulation, before entering the circular air inlet the air volume (Fig. 2) has an elliptical section with minor and major diameters of 18 and 25 mm, respectively ($A_o = 353$ mm^2). This area is equivalent to a circle with $D = 21.2$ mm, that has to reduce to the air inlet circle with $d = 18$ mm. From Eq. (2) the air compression ratio becomes $\eta = 0.85$. The airflow through the inlet is 730 l/min at 125 km/h, i.e. 525.6 l/min at 90 km/h, exceeding the rider requirement of 134.4 l/min for sprint purposes.

4.2 Positioning and geometry influence of the rear vent

From the air velocity contour plot in Fig. 8(a), the location of the rear vent created an interference with the external air flow. Fig. 6(b) shows that the minimum pressure gradient
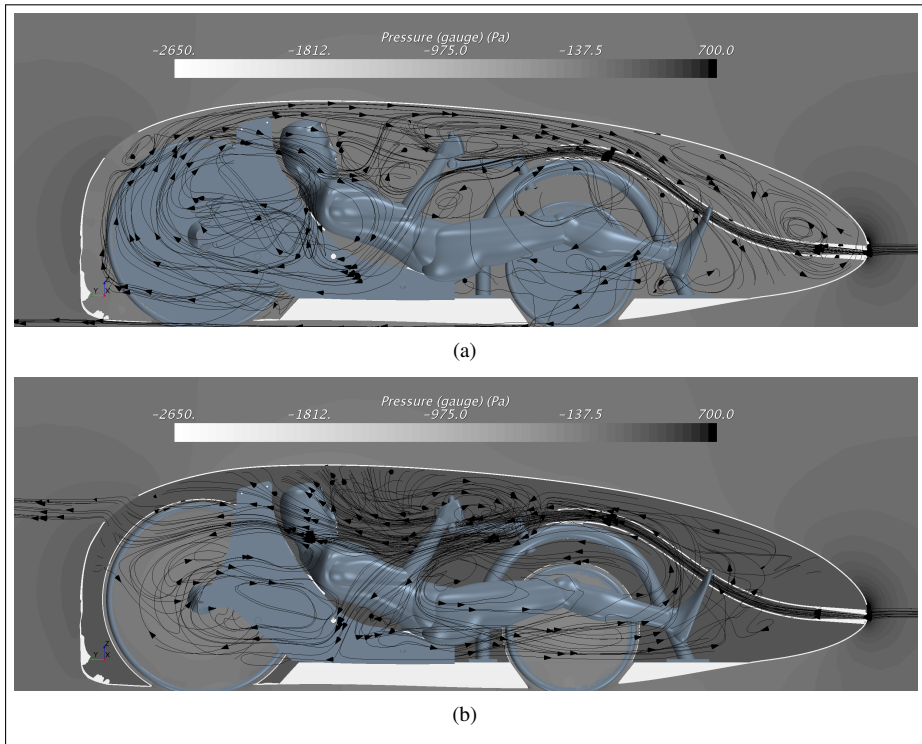
Fig. 6 Pressure and internal flow with models A (a) and B (b), i.e. without and with wheel-covers.
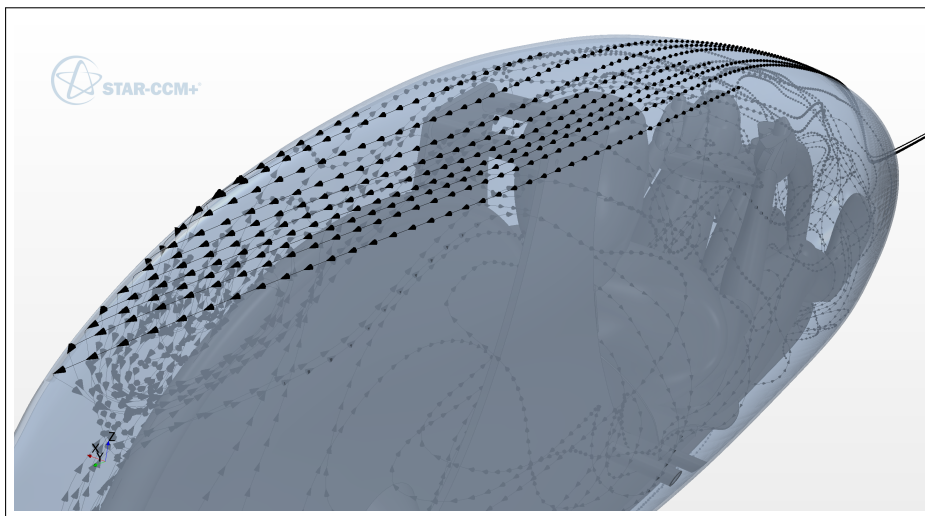

Fig. 7 Streamlines entering through the air outlet in model A.

between internal and external air is located at H = 420 mm. The air outlet was moved to this position in model C to minimize interference with the external flow.

Moving the outlet from H = 660 mm (model B) to H = 420 mm (model C) lowered the drag power by 11 W at 125 km/h. Fig. 8(a) and Fig. 8(b) provide a visual comparison of the tail wake, which is reduced with the new position of the rear vent.

A maximum reduction of 5 W in aerodynamic power was found within the design space for the air outlet geometry. This reduction is below the CFD confidence of 7 W and suggests that the rear vent geometry could play a negligible role.
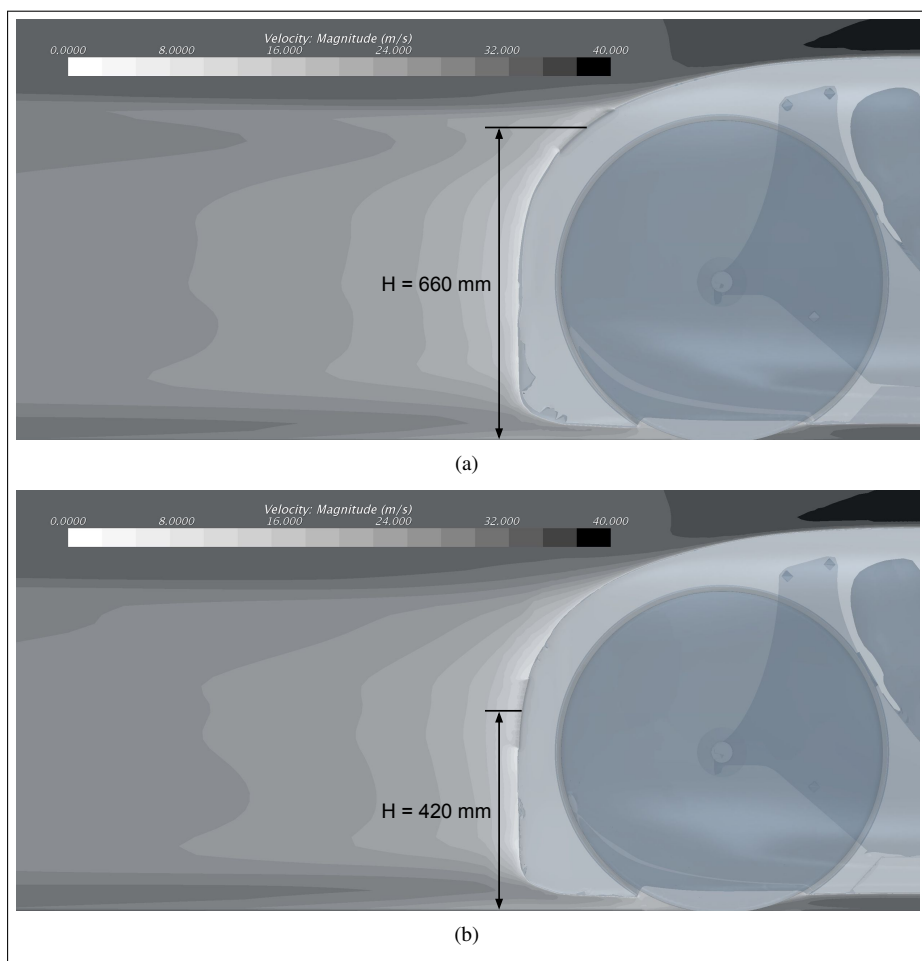

Fig. 8 Near tail wake velocity for models B (a) and C (b).

5 Conclusions

The problem of internal ventilation in fully faired HPVs has been considered with focus on high-speed prototypes. An analytical approach has been proposed to calculate the air inlet size by considering the oxygen consumption of the rider in maximal effort conditions. An CFD simulation has been implemented to compare subcases having different design solutions with respect to wheel-covers, location of the rear vent and its geometry.

Uncovered wheels can compromise the intended behaviour of the air outlet by generating unwanted recirculation flow inside the vehicle. The implementation of internal wheel-covers can improve the HPV efficiency by lowering the aerodynamic power loss up to 23 W at 125 km/h. Moreover, it emerged that positioning of the rear vent can provide a minor but significant improvement of 11 W at 125 km/h. The air outlet geometry appears to have a negligible effect within the considered ranges of size and aspect ratio.

References

1. T. Kobayashi, K. Kitoh, SAE Technical Paper **920338** (1992). DOI 10.4271/920338

2. M.N. Dhaubhadel, Journal of Fluids Engineering **118**(4), 647 (1996). DOI 10.1115/1.2835492

3. C.L. Rumsey, S.X. Ying, Progress in Aerospace Sciences **38**(2), 145 (2002). DOI 10.1016/ S0376-0421(02)00003-9

4. K. Fujii, Progress in Aerospace Sciences **41**(6), 455 (2005). DOI j.paerosci.2005.09.001

5. D. Nicolopoulos, E. Berton, G. Gouvernet, A. Jacques, Sports Eng **11**(4), 177 (2009). DOI 10.1007/ s12283-009-0022-7

6. J. Banks, A.B. Phillips, S.R. Turnock, D.A. Hudson, D.J. Taunton, Proc IMechE Part P: Journal of Sports Engineering and Technology **228**(1), 49 (2014). DOI 10.1177/1754337113493847

7. A. Coppel, T.N. Gardner, N. Caplan, D.M. Hargreaves, Proc IMechE Part P: Journal of Sports Engineering and Technology **224**(1), 25 (2010). DOI 10.1243/17543371JSET37

8. A. Sliasas, S. Tullis, Sports Eng **12**(1), 31 (2009). DOI 10.1007/s12283-009-0026-3

9. A. Sliasas, S. Tullis, Proc IMechE Part P: Journal of Sports Engineering and Technology **224**(1), 9 (2010). DOI 10.1243/17543371JSET57

10. B. Bixler, S. Riewald, J Biomech **35**(5), 713 (2002). DOI http://dx.doi.org/10.1016/S0021-9290(01) 00246-9

11. A. Rouboa, A. Silva, L. Leal, J. Rocha, F. Alves, J Biomech **39**(7), 1239 (2006). DOI http://dx.doi.org/ 10.1016/j.jbiomech.2005.03.012

12. A.N. Hayati, H. Ghaffari, M. Shams, Proc IMechE Part P: Journal of Sports Engineering and Technology (2015). DOI 10.1177/1754337115598488

13. B. Blocken, T. Defraeye, E. Koninckx, J. Carmeliet, P. Hespel, Computers & Fluids **71**, 435 (2013). DOI 10.1016/j.compfluid.2012.11.012

14. B. Blocken, Y. Toparlar, J Wind Eng Ind Aerodyn **145**, 178 (2015). DOI 10.1016/j.jweia.2015.06.015

15. T. Defraeye, B. Blocken, E. Koninckx, P. Hespel, J. Carmeliet, J Biomech **43**(7), 1262 (2010). DOI 10.1016/j.jbiomech.2010.01.025

16. T. Defraeye, B. Blocken, E. Koninckx, P. Hespel, J. Carmeliet, J Biomech **43**(12), 2281 (2010). DOI 10.1016/j.jbiomech.2010.04.038

17. T. Defraeye, B. Blocken, E. Koninckx, P. Hespel, J. Carmeliet, J Biomech **44**(9), 1695 (2011). DOI 10.1016/j.jbiomech.2011.03.035

18. T. Defraeye, B. Blocken, E. Koninckx, P. Hespel, P. Verboven, B. Nicolai, J. Carmeliet, J Biomech **136**(1), 011005 (2013). DOI 10.1115/1.4025792

19. D. Fintelman, H. Hemida, M. Sterling, F.X. Li, J Wind Eng Ind Aerodyn **144**, 31 (2015). DOI 10.1016/j.jweia.2015.05.009. Selected papers from the 6th International Symposium on Computational Wind Engineering {CWE} 2014

20. M.D. Griffith, T. Crouch, M.C. Thompson, D. Burton, J. Sheridan, N.A.T. Brown, J Fluid Eng - T ASME **136**(10), 101105 (2014). DOI 10.1115/1.4027428

21. Website http://www.ihpva.org accessed on April 24th, 2017

22. Website http://www.whpva.org accessed on April 24th, 2017

23. T. Prebble. More positive data from leisure trends group (2012). The Recumbent Journal, website http://www.recumbentjournal.com accessed on September 1th, 2016

24. T. Prebble. Recumbents on the rise according to leisure trends group (2012). The Recumbent Journal, website http://www.recumbentjournal.com accessed on September 1th, 2016

25. T. Prebble. Trikes are the wave of the future (2013). The Recumbent Journal, website http://www.recumbentjournal.com accessed on September 1th, 2016

26. Website http://recumbents.com/wisil/whpsc2016/speedchallenge.htm accessed on April 24th, 2017

27. J. Nobile, Human Power **6**(2), 5 (1987)

28. M. Drela, Human Power **11**(3), 23 (1994)

29. W.B. Schreur, Human Power eJournal (2004). Available at http://www.hupi.org - Accessed on April 5th, 2016

30. C.R. Kyle, M.D. Weaver, Proc IMechE Part A: Journal of Power and Energy **218**(3), 141 (2004). DOI 10.1243/095765004323049878

31. H. Gong, P.W. Bradley, M.S. Simmons, D.P. Tashkin, Am Rev Respir Dis **134**(4), 726 (1986). DOI 10.1164/arrd.1986.134.4.726

32. Website http://mdx.plm.automation.siemens.com/star-ccm-plus accessed on April 24th, 2017

33. P. Malan, K. Suluksna, E. Juntasaro, in *47th AIAA Aerospace Sciences Meeting* (2009), pp. 5–8

34. P. Spalart, S. Allmaras, in *30th aerospace sciences meeting and exhibit* (1992), p. 439

35. P. Baldissera, C. Delprete, Int J Mech Control **17**(2), 27 (2016)

36. P. Baldissera, Proc IMechE Part P: Journal of Sports Engineering and Technology (In press). DOI 10.1177/1754337116658587

37. W. Hennekam, J. Bontsema, Eur J Phys **12**(2), 59 (1991)

38. W. Hennekam, M. Govers, Phys Educ **31**(5), 320 (1996)

39. H. Schlichting, K. Gersten, E. Krause, H. Oertel, K. Mayes, *Boundary-layer theory*, vol. 7 (Springer, 1960)

List of Figures

List of Tables